FEASIBILITY STUDY OF A PULSED SOLENOID FOR BNL-E951 TARGETRY PROGRAM

K. McDonald[a], J. Minervini[b], R. Titus[b], R. Fernow[c], J. Gallardo[c], M. Iarocci[c], S Kahn[c], H. Kirk[c], I. Marneris[c], R. Samulyak[c], N. Simos[c], P. Thieberger[c], R. Weggel[c],
[a]Princeton University, Princeton, NJ 08544
[b]MIT, Cambridge, MA 02139
[c]BNL, Upton, NY 11973

March 29, 2002

Contents

List of Figures

List of Tables

Chapter 1

Executive Summary

1.1 Acknowledgment

Muon Collaboration

Chapter 2

Introduction and Overview

Chapter 3

Previous Experiments

3.1 Target Studies

3.1.1 Introduction

A successful Muon Collider or Neutrino Factory based on a muon storage ring requires the production of copious pions which are then conducted into a decay channel where the muon decay products are collected.

Current scenarios require intense protons beams, suitable target material and a high-field solenoidal field which surrounds the target. Modeling studies point to high-Z materials being more efficient at producing pions of both signs, whereas low-Z materials are better in avoiding the absorption of the produced pions. Carbon has the advantage of permitting larger target cross-sections and therefore larger beam spot sizes with a corresponding decrease in shock heating due to high peak energy depositions.

The Muon Collider Collaboration is considering another approach, however, which is to retain the pion production advantage from high-Z materials by utilizing a free liquid mercury jet. In this case, the jet can be conveniently replaced so that target integrity after exposure to the proton beam is not an issue. However, the dynamics of a mercury jet moving in a high-field solenoid field followed by its dispersion after the interaction with the intense proton beam, remains to be studied.

For this reason, E951 [1] has been proposed and approved for running at the Brookhaven Alternating Gradient Synchrotron (AGS).

3.1.2 Experimental layout

The A3 beam line [2] (See Fig. 3.1) in the experimental hall has been configured for the transport of primary 24 GeV protons extracted from the AGS. All targets have been mounted inside a stainless steel vessel which prevents the potential dispersal of activated fragments which could be ejected from the tested target. This target system is placed on a translation table (Fig. 3.2) which has a target flag mounted to one side to facilitate the tuning of the proton beam prior to the target being moved into position.

Beam spot sizes were subsequently measured by placing unexposed film emulsion on beam windows which were placed interior to one of the secondary containment vessel in order to test the integrity of the beam windows before the subsequent exposure of our targets. Measured beam rms spot sizes are σ_x= 1.0 mm and σ_y= 0.3 mm (See Fig. 3.4).

Muon Collaboration

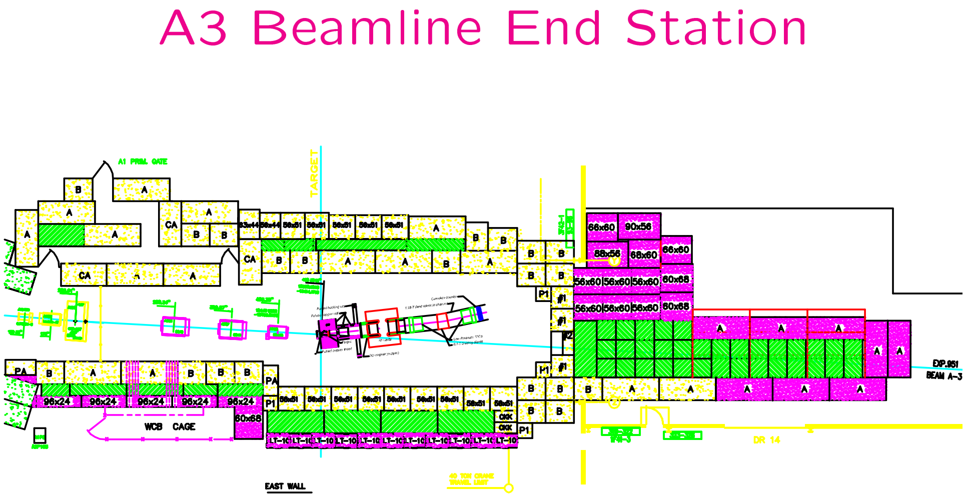

Figure 3.1: The AGS A3 beam line

Beam intensities were monitored by a series of beam transformers extending from the AGS extraction point to immediately preceding the target table. Intensities were adjustable from 0.5 to 4.0 $\times 10^{12}$ protons/pulse with full bunch beam lengths typically 150 ns.

The dispersal of the mercury was recorded with the use of two independent camera systems: 1) an Olympus Industrial, Encore PCI 8000S camera system capable of recording at a rate of 4 kHz with shutter settings for each frame set to 25 μs; and 2) an SMD 64K1M camera capable of taking 16 frames at speeds of up to 1 MHz. The exposure time for the latter camera is 150 ns per frame.

Strain measurements were based on miniaturized Fabry-Perot interferometers provided by Fiso Technologies. Signals from the interferometers were then processed through a Veloce multi-channel system.

3.1.3 Carbon Targets

Two forms of solid carbon rods were exposed to the primary proton beam: 1) two ATJ carbon rods each 30 cm long by 16 mm diameter; and 2) two 12 cm long by 16 mm diameter rods made from an anisotropic carbon-carbon composite.

The carbon composite is particularly interesting because its elastic modulus is unusually high while its coefficient of thermal expansion is nearly zero

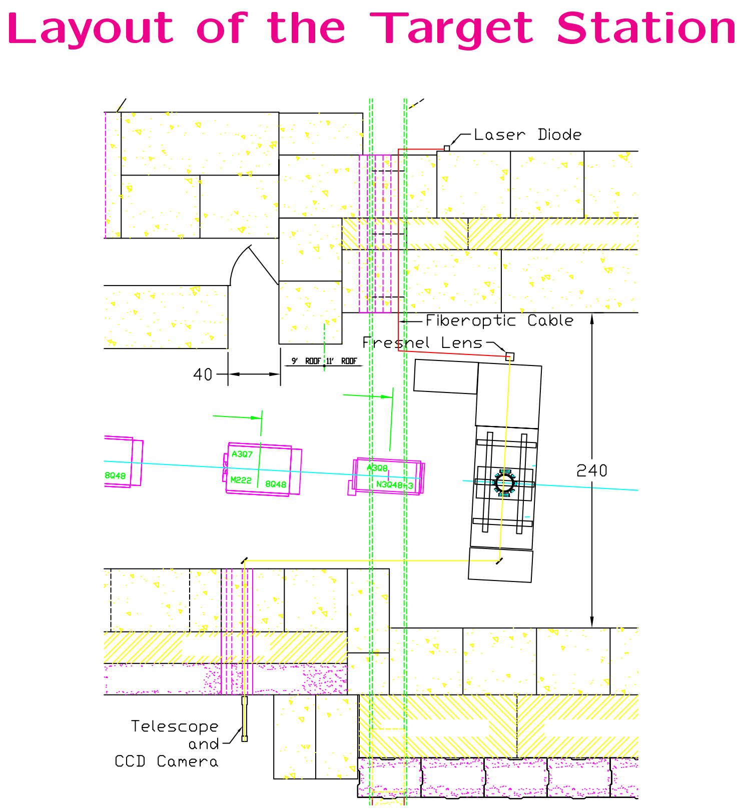

Figure 3.2: The A3 beam line target station

over a large temperature range. See Table 3.1 for the relevant properties.

In Fig. 3.4, results of two strain measurements for both materials are

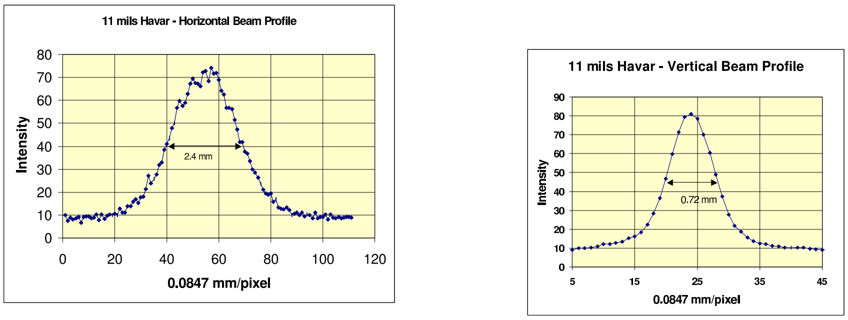

Figure 3.3: The A3 beam spot size projections

shown. From the ATJ strain waveform we see clear evidence of a 100 kHz signal superimposed on a 4.5 kHz signal which has an initial peak-to-peak amplitude of 30 μstrains. Also clearly seen, before the arrival of the proton pulse, is the background noise level of the strain gauge which is $\sigma_{rms}=$ 0.7 μstrains. The 4.5 kHz signal corresponds well to the expected longitudinal propagation of reflected pressure waves. The 100 kHz signal is appropriate for radial reflections. For the carbon-carbon composite we observe a 34 kHz signal but with a much lower amplitude. This signal's initial peak-to-peak level is 3 μstrains while the background noise level for this strain gauge is $\sigma_{rms}=$ 0.3 μstrains.

3.1.4 Mercury Targets

Two separate mercury targets were exposed to the AGS proton beam. An initial test was made with a passive system in which a small well loaded with 1.9 cm^3 of mercury was placed into a container in which the dispersed mercury droplets could be collected and channeled back into the well. Five shots

Table 3.1: Properties of carbon targets

	ATJ	Carbon-Carbon Composite Z	Carbon-Carbon Composite (U,V)
Elastic Modulus, GPa	9.6	117	48
Exp. coefficient, 1/°C	2.46×10^{-6}	$\sim$0	$\sim$0

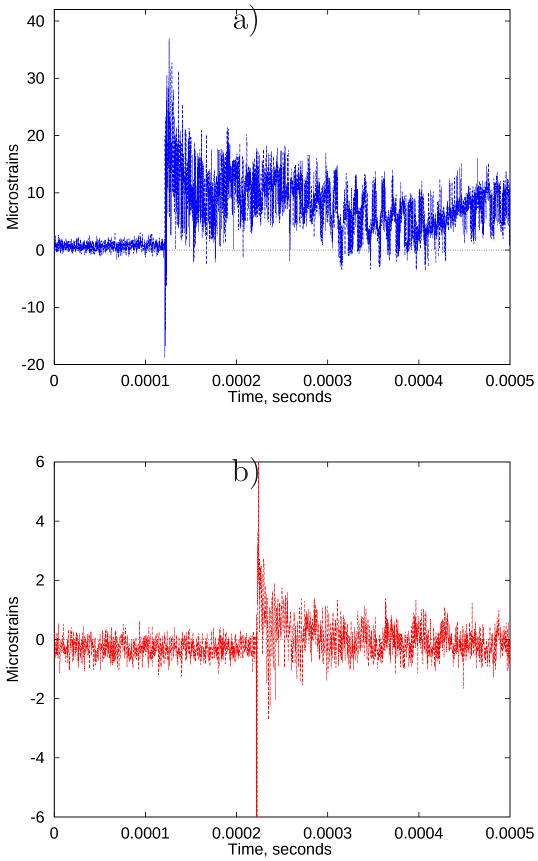

Figure 3.4: Strain gauge data from carbon targets: a) 3×10^{12} proton beam on ATJ carbon; b) 2×10^{12} proton beam on carbon-carbon composite

were delivered and the mercury dispersion recorded. The beam intensity for these shots varied from 0.65 to 4 $\times 10^{12}$. In Fig. 3.5 we see three frames taken with the SMD 16K1M camera. The initial velocity of the ejected mercury was 70 m/s, however, this velocity was reduced to 40 m/s by the time the cloud of mercury has traveled 4 cm. This effect could be due to the presence of 1 atmosphere of air inside the chamber.

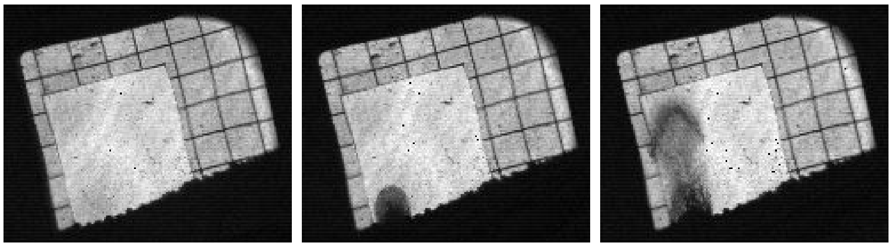

a) b) c)

Figure 3.5: Hg interaction with 24 GeV, 4×10^{12} protons; $t =$ a) 0 μs; b) 300 μs; c) 800 μs. The grid is 1 cm x 1 cm.

The mercury jet (Fig. 3.6) was formed by supplying a pneumatic pressure of 26 psi which forced the mercury out of a 1 cm diameter nozzle inclined at 18.5°. The resulting mercury stream travels 20 cm to its maximum height at which point the trajectory of the Hg jet overlaps with the proton beam for 19 cm. The average velocity of the jet was 2.5 m/s. The diameter of the jet at the interaction point fluctuated between 0.7 and 1.7 cm.

Dispersal of the mercury by energy deposition due to the interacting proton beam was observed directly by viewing prominences as they left the bulk of the mercury jet. We were also able to indirectly measure the velocity of Hg droplets, since their arrival at the quartz viewing ports was signaled by distinctive splashes. Directly measured bulk velocities range from 5 to 50 m/s while the velocities of the Hg droplets arriving at the quartz window varied from 1 to 10 m/s. In both cases we observe that the maximum velocities increase roughly proportionally to the intensity of the impinging proton beam.

Also of interest is the extent of the disruption of the mercury, and in particular whether this disruption extends forward and backward from the interaction region. It was observed that the region of disruption was confined largely to the volume of overlap with the proton beam with no evidence of jet dispersal propagating back to the nozzle. The maximum disruption length observed was 14 cm.

Finally, by utilizing the SMD 64K1M camera set in a fast frame mode (1 frame/10 μs), we observed that the breakup of the mercury jet commenced after an elapsed time of $\sim$40 μs. Observations with the camera set as fast as 18 frames per 18 μs showed no discernible disruptive motion in the jet.

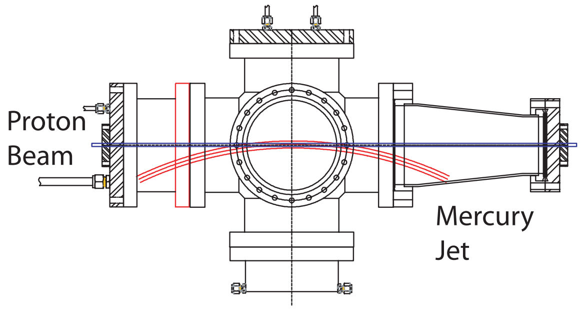

Figure 3.6: Elevation view of the Hg jet overlapping with the 24 GeV proton beam.

3.1.5 Summary

The E951 collaboration has begun a series of measurements with the goal of providing observations needed to clarify the best technological path for the Neutrino Factory and Muon Collider Collaboration to proceed in order to provide a future machine with a source of muons more intense than presently achievable.

Among the initial results:

- The strain amplitudes for a cylinder made from an anisotropic carbon-carbon composite are substantially less (a factor of $\sim$10) than those for ATJ carbon.
- Hg jet dispersal is mostly transversal. The jet disruption is confined mostly to the proton beam-Hg jet interception volume.
- For a 4×10^{12} proton beam, dispersed Hg droplet velocities are $<$ 10 m/s.
- Hg jet dispersal is delayed for $\sim$40 μs.

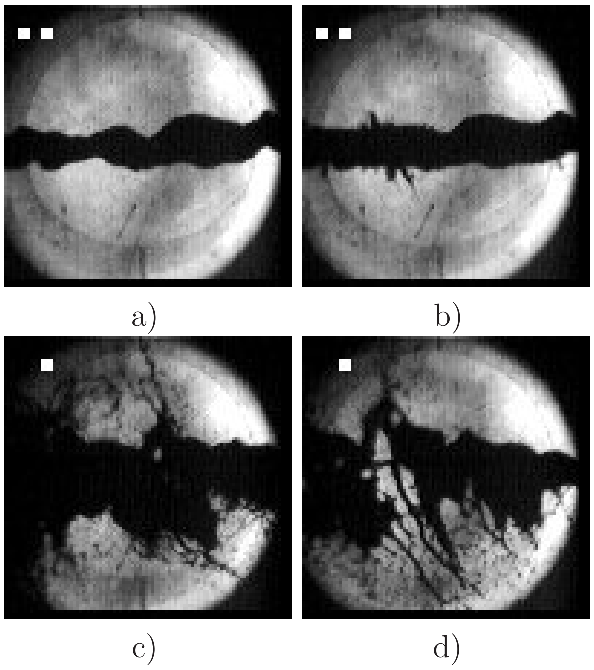

Figure 3.7: Hg jet interaction with 24 GeV 3.8×10^{12} protons; $t =$ a) 0 ms; b) 0.75 ms; c) 10 ms; d) 18 ms

Goals for subsequent runs include increasing the single pulse proton beam intensity to the level of 16×10^{12} (16 TP) and the addition of an high-field solenoidal field surrounding the target in order to ascertain the influence of the magnetic field on the incident Hg jet and the subsequent dispersal of the mercury.

Bibliography

[1] James Alessi, et al., *An R&D Program for Targetry and Capture at a Muon-Collider Source*, Proposal submitted to Brookhaven National Laboratory, (Sept. 28, 1998).

[2] K. Brown, *First Beam Tests of the Muon Collider Target Test Beam Line at the AGS*, Proceedings of the 2001 Particle Accelerator Conference, Chicago, IL, June 18-22, 2001.

Chapter 4

Simulations

4.1 Numerical Simulation of the Muon Collider Target

The numerical simulation of hydro- and magnetohydrodynamics processes in the Muon Collider target is needed for better understanding of the physics involved and for answering engineering design questions. The Muon Collider target will contain a series of mercury jet pulses of about 0.5 cm in radius and 60 cm in length. Each pulse will be shot at a velocity of 30-35 m/sec into a 20 Tesla magnetic field at a small angle (0.1 rad) to the axis of the field. When the jet reaches the center of the magnet, it is hit with 3 ns proton pulses arriving with 20 ms time period; each proton pulse will deposit about 100 J/g of energy in the mercury.

The main issues of the target design addressed in our numerical studies are the distortion of the jet due to eddy currents as it propagates through the magnetic coil, the deformation of the jet surface due to strong pressure waves caused by the proton pulses and the probability of the jet breakup. Studying the state of the target during its interaction with proton pulses will help to achieve the maximal proton production rate and therefore an optimal target performance.

4.1.1 Magnetohydrodynamics of Free Surface Liquid Flows

The basic set of equations describing the interaction of a compressible conducting fluid flow and a magnetic field is contained in Maxwell's equations and in the equations of fluid dynamics suitably modified [1, 11]. Namely, the systems contains the mass, momentum and energy conservation equations for the fluid which have hyperbolic nature and a parabolic equation for the evolution of the magnetic field.

$$\frac{\partial \rho}{\partial t} = -\nabla \cdot (\rho \mathbf{u}), \tag{4.1}$$

$$\rho \left(\frac{\partial}{\partial t} + \mathbf{u} \cdot \nabla \right) \mathbf{u} = -\nabla P + \rho \mathbf{X} + \frac{1}{c} (\mathbf{J} \times \mathbf{B}), \tag{4.2}$$

$$\rho \left(\frac{\partial}{\partial t} + \mathbf{u} \cdot \nabla \right) U = -P \nabla \cdot \mathbf{u} + \frac{1}{\sigma} \mathbf{J}^2 - \frac{1}{c} \mathbf{u} \cdot (\mathbf{J} \times \mathbf{B}), \tag{4.3}$$

$$\frac{\partial \mathbf{B}}{\partial t} = \nabla \times (\mathbf{u} \times \mathbf{B}) - \nabla \times (\frac{c^2}{4\pi\sigma} \nabla \times \mathbf{B}), \quad (4.4)$$

$$\nabla \cdot \mathbf{B} = 0, \quad (4.5)$$

Here $\mathbf{u}$, ρ and U are the velocity, density and total energy of the fluid, respectively, P is the total stress tensor, $\mathbf{X}$ includes external forces of non-magnetic origin, $\mathbf{B}$ is the magnetic field induction, $\mathbf{J}$ is the current density distribution and σ is the fluid conductivity. The magnetic field $\mathbf{H}$ and magnetic induction $\mathbf{B}$ are related by the magnetic permeability coefficient μ: $\mathbf{B} = \mu \mathbf{H}$.

The system (4.1-4.4) must be closed with an equation of state. We are especially interested in fluid behavior under extreme thermodynamics conditions. Some related equation of state models are discussed below.

The following boundary conditions must be satisfied at the jet surface:

i) the normal component of the velocity field is continuous across the material interface.

ii) the normal and tangential components of the magnetic field at the material interface are related as

$$\mathbf{n} \cdot (\mathbf{B}_2 - \mathbf{B}_1) = 0, \quad (4.6)$$

$$\mathbf{n} \times (\mathbf{H}_2 - \mathbf{H}_1) = \frac{4\pi}{c} \mathbf{K}, \quad (4.7)$$

where $\mathbf{K}$ is the surface current density. The above jump conditions define the refraction of magnetic lines on the material interface. We can assume $\mu = 1$ for most fluids. Notice that the surface current density $\mathbf{K}$ corresponds to a current localized in a thin fluid boundary layer (δ-functional current) which is non-zero only for superconducting materials. The current density in fluids at normal conditions is distributed in the 3D volume and $\mathbf{K} = 0$. Therefore, the equations (4.6,4.7) simply require the continuity of the normal and tangential components of the magnetic field.

The behavior of a fluid in the presence of electromagnetic fields is governed to a large extent by the magnitude of the conductivity. For fluid at rest (4.4) reduces to the diffusion equation

$$\frac{\partial \mathbf{B}}{\partial t} = \frac{c^2}{4\pi\mu\sigma} \Delta \mathbf{B} \quad (4.8)$$

This means that an initial configuration of magnetic field will decay with typical diffusion time

$$\tau = \frac{4\pi\mu\sigma L^2}{c^2},$$

where L is a characteristic length of the spatial variation of $\mathbf{B}$. Despite being good enough conductors, most of liquid metals including mercury are characterized by small diffusion times (33 microseconds for a mercury droplet of 1 cm radius) compared to some solid conductors (1 sec for a copper sphere of 1 cm radius). Therefore the magnetic field penetration in such liquid conductors can be considered as an instantaneous process.

Another crucial phenomena for MHD flows of compressible conducting fluids is the propagation of Alfven waves. For mercury at room temperature the Alfven velocity

$$\mathbf{v}_A = \frac{\mathbf{B}_0}{\sqrt{4\pi\rho_0}},$$

where $\mathbf{B}_0$ and ρ_0 are unperturbed (mean) values of the magnetic induction and density of the fluid, respectively, is $[B_0(\text{Gauss})/13.1]$ cm/sec. This is a small number compared with the speed of sound of 1.45×10^5 cm/sec even for the magnetic field of 20 T. In many cases, however, it is not desirable to compute Alfven waves explicitly in the system. If, in addition, both the magnetic field diffusion time and the eddy current induced magnetic field are small, an assumption of the constant in time magnetic field can be made. The current density distribution can be obtained in this case using Ohm's law

$$\mathbf{J} = \sigma\left(-\text{grad}\phi + \frac{1}{c}\mathbf{u}\times\mathbf{B}\right). \tag{4.9}$$

Here ϕ is the electric field potential. The potential ϕ satisfies the following Poisson equation

$$\Delta\phi = \frac{1}{c}\text{div}(\mathbf{u}\times\mathbf{B}), \tag{4.10}$$

and the Neumann boundary conditions

$$\left.\frac{\partial\phi}{\partial\mathbf{n}}\right|_\Gamma = \frac{1}{c}(\mathbf{u}\times\mathbf{B})\cdot\mathbf{n},$$

where $\mathbf{n}$ is a normal vector at the fluid boundary Γ. This approach is applicable for the study of a liquid metal jet moving in a magnetic field.

We shall use also the following simplification for the modeling of a thin jet moving along the solenoid axis. Let us consider a ring of liquid metal of radius r that is inside a thin jet moving with velocity u_z along the axis of a solenoid magnet. The magnetic flux $\Phi = \pi r^2 B_z$ through the ring varies with time because the ring is moving through the spatially varying magnetic field, and because the radius of the ring is varying at rate $u_r = dr/dt$. Therefore, an azimuthal electric field is induced around the ring:

$$2\pi r E_\phi = -\frac{1}{c}\frac{d\Phi}{dt} = -\frac{\pi r^2}{c}\frac{dB_z}{dt} - \frac{2\pi r u_r B_z}{c}$$
$$= -\frac{\pi r^2 u_z}{c}\frac{\partial B_z}{\partial z} - \frac{2\pi r u_r B_z}{c}.$$

This electric field leads to an azimuthal current density

$$J_\phi = \sigma E_\phi = -\frac{\sigma r u_z}{2c}\frac{\partial B_z}{\partial z} - \frac{\sigma u_r B_z}{c}, \tag{4.11}$$

which defines the Lorentz force in the momentum equation (4.2) and leads to the distortion of the jet moving in a non-uniform magnetic field.

The linear stability analysis of thin conducting liquid jets moving along the axis of a uniform magnetic field [1] and the corresponding analysis for the Muon Collider target [7] show that an axial uniform field tends to stabilize the jet surface. The influence of a strong nonuniform field must be studied by means of the numerical simulation.

4.1.2 Numerical Implementation

In this section, we shall describe numerical ideas implemented in the FronTier MHD code. FronTier represents interfaces as lower dimensional meshes moving through a volume filling grid [5]. The traditional volume filling finite difference grid supports smooth solutions located in the region between interfaces. The location of the discontinuity and the jump in the solution variables are defined on the lower dimensional grid or interface. The dynamics of the interface comes from the mathematical theory of Riemann solutions, which is an idealized solution of a single jump discontinuity for a conservation law. Where surfaces intersect in lower dimensional objects (curves in three dimensions), the dynamics is defined by a theory of higher dimensional Riemann problems such as the theory of shock polars in gas dynamics. Nonlocal correlations to these idealized Riemann solutions provide the coupling between the values on these two grid systems.

The computation of a dynamically evolving interface requires the ability to detect and resolve changes in the topology of the moving front. A valid interface is one where each surface and curve is connected, surfaces only intersect along curves and curves only intersect at points. We say that such an interface is untangled. Two independent numerical algorithms, grid-based tracking and grid-free tracking, were developed [5, 6] to resolve the untangling problem for the moving interface. The advantages and deficiencies of the two methods are complementary and an improved algorithm combining them into a single hybrid method was implemented in the FronTier code and described in [6].

We solve the hyperbolic subsystem of the MHD equations, namely the equations (4.1-4.3), on a finite difference grid in both domains separated by the free surface using FronTier's interface tracking numerical techniques. Some features of the FronTier hyperbolic solvers include the use of high resolution methods such as MUSCL, Godunov and Lax-Wendroff with a large selection of Riemann solvers such as the exact Riemann solver, the Colella-Glaz approximate Riemann solver, the linear US/UP fit (Dukowich) Riemann solver, and the Gamma law fit. We use realistic models for the equation of state such as the polytropic and stiffened polytropic equation of state, the Gruneisen equation of state, and the SESAME tabular equation of state.

The evolution of the free fluid surface is obtained through the solution of the Riemann problem for compressible fluids [5, 13]. Notice that since we are primarily interested in the contact discontinuity propagation, we do not consider the Riemann problem for the MHD system and therefore neglect elementary waves typical for MHD Riemann solutions.

We have developed the following numerical approaches for solving the equation (4.4) for the magnetic field evolution and the Poisson equation (4.10):

Finite difference solvers based on regular grids. We have developed a parallel elliptic solver for the current density distribution equation (refeq10) based on finite difference technique on rectangular grid in regular domains. We have performed smoothening of discontinuities of physics fields and applied the cubic spline interpolation of the fields within several grid blocks. The corresponding parallel iterative solvers for linear systems of equations explore different Krylov subspace and preconditioning methods and are based on PETSC libraries [14]. The solver is very effective for modeling multifluid MHD phenomena for fluids with smooth interfaces without small length scale perturbations. For MHD flows with unstable interfaces, we use FE solvers on meshes dynamically conforming to evolving interfaces.

Finite element solvers. Finite element solvers are based on grids dynamically conforming to the moving interface. The grid generation method is based on the point-shifted grid technique of McBryan [12]. For the elliptic and parabolic systems considered here we favor the mixed-hybrid finite element formulation of Chavent and Jaffre [2]. We utilize Glowinski-Wheeler domain decomposition [8]. The linear systems obtained for the subdomain ”interior problems” are solved using direct methods which preconditioned conjugate gradients for the global ”wire basket” problem. Preconditioners such as vector probing and balancing are used.

4.1.3 Modeling Thermodynamics Properties of Fluids

Material properties strongly influence the structure and dynamics of waves in any continuous mechanical system. In particular, elementary waves in compressible fluids defined by Riemann problems depend both quantitatively and qualitatively on the property of an EOS.

SESAME equation of state for mercury. To model accurately the interaction of the mercury target with proton pulses, we created a tabulated equation of state for mercury in a wide temperature - pressure domain which includes the liquid-vapor phase transition and the critical point. The FronTier code uses SESAME Equation-of-Setate Library [9], developed at Los Alamos National Laboratory, to work with such tabulated EOS format. Necessary data describing thermodynamic properties of mercury were obtained courtesy of T. Trucano of Sandia National Laboratory. The behavior of isotherms of the specific internal energy, pressure and entropy of mercury obtained using this equation of state are shown in Figures 4.1 - 4.3. The computational domain included the two phase region for mercury and the critical point.

Isentropic EOS for cavitation flows. The tabulated EOS model allows an accurate description of equilibrium thermodynamic processes in mercury. However processes which occur in the mercury jet interacting with proton pulses go beyond the assumptions of equilibrium thermodynamics. Namely a regions of negative pressure (liquid tension) appear during the interaction which lead to the formation of cavities. To resolve such problem of negative pressures, we have developed an analytic two phase EOS model for an isentropic regime of the flow. The model is based on the polytropic EOS for the gas phase, the stiffened polytropic EOS for the liquid phase [13] and the following EOS type model (pressure - density relation):

$$P = P_l^{sat} + P_{gl} \log \left[\frac{\rho_g a_g^2 (\rho_l + \alpha(\rho_g - \rho_l))}{\rho_l(\rho_g a_g^2 - \alpha(\rho_g a_g^2 - \rho_l a_l^2))} \right], \tag{4.12}$$

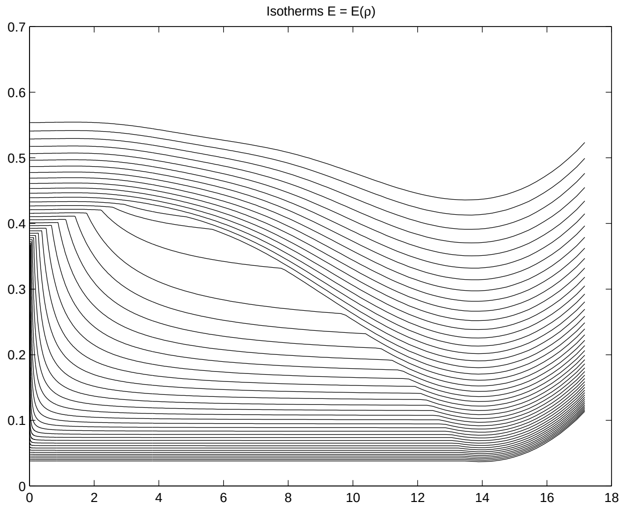

Figure 4.1:]
Isotherms of mercury specific internal energy as a function of density in the mixed liquid - vapor domain.

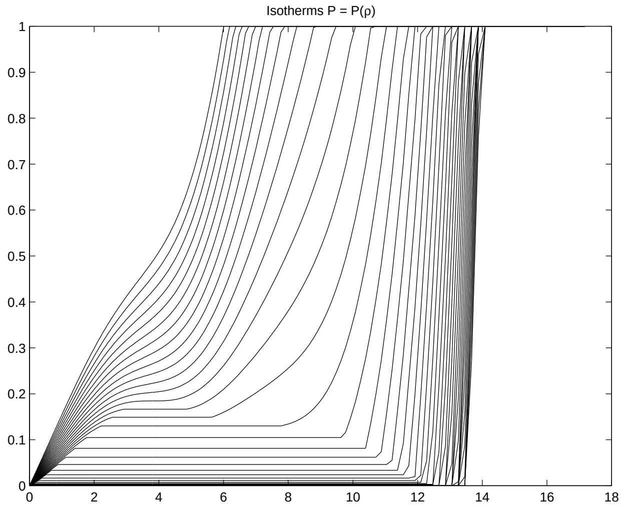

Figure 4.2: Isotherms of mercury pressure as a function of density in the mixed liquid - vapor domain.

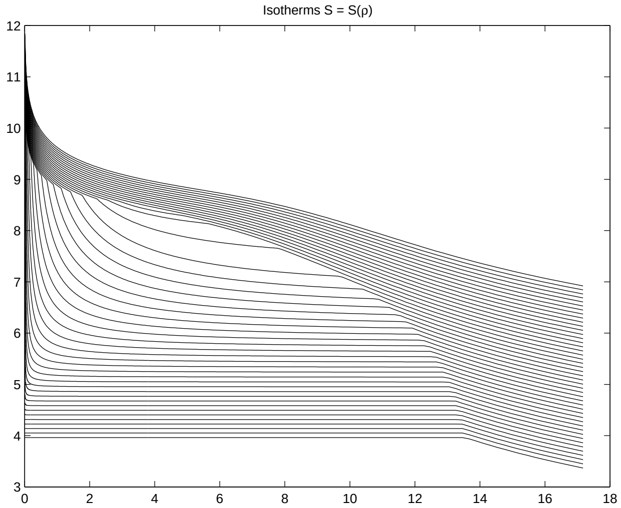

Figure 4.3: Isotherms of mercury entropy as a function of density in the mixed liquid - vapor domain.

where

$$P_{gl} = \frac{\rho_g a_g^2 \rho_l a_l^2 (\rho_g - \rho_l)}{\rho_g^2 a_g^2 - \rho_l^2 a_l^2},$$

Here ρ_g, p_g, a_g, ρ_l, p_l, a_l are the density, pressure, and sound speed of the saturated gas and liquid respectively, and the void fraction α is

$$\alpha = \frac{\rho - \rho_l}{\rho_g - \rho_l}.$$

We have developed the corresponding software library for FronTier.

4.1.4 Numerical Simulation Results

MHD studies of the Muon Collider target We shall present here numerical simulation results of thin jets of conducting fluid moving in highly nonuniform magnetic fields. In this numerical experiment, a 1 cm radius liquid jet is sent into a 20 T solenoid with the velocity 90 m/sec along the solenoid axis. The density of the liquid is $1\, g/cm^3$, the electric conductivity is 10^{16} in Gaussian units, and the initial pressure in the liquid is 1 atm. The electrically and magnetically neutral gas outside the jet has density 0.01 g/cm and the same initial pressure. The thermodynamic properties of the

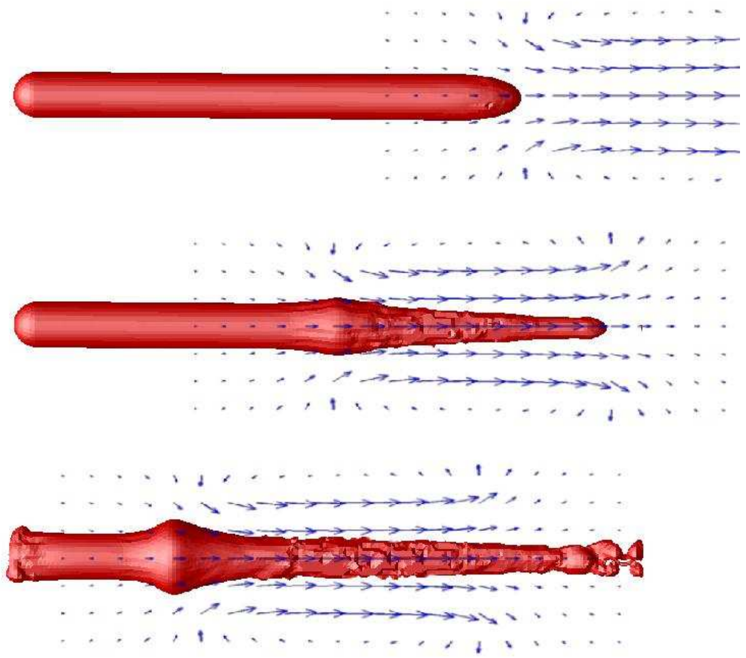

Figure 4.4: Liquid metal jet in a 20 T solenoid.

ambient gas were modeled using the polytropic equation of state [4] with the ratio of specific heat $\gamma = 1.4$ and the ideal gas constant $R = 1$. The properties of the liquid jet were modeled using the stiffened polytropic equation of state with the Gruneisen exponent = 5 and the stiffened gas constant $P_\infty = 3 \cdot 10^9 g/(cm \cdot sec^2)$. The field of a magnetic coil of rectangular profile and $8 \times 8 \times 20$ cm size was calculated using exact analytical expressions.

A set of images describing the evolution of the liquid jet as it enters and leaves the solenoid is depicted in Figure 4.4. The strong nonuniform magnetic field near the solenoid entrance squeezes and distorts the jet. The magnetic field outside the solenoid stretches the jet which results in the jet breakup. Notice that these simulations use the expression for the current density distribution (4.11) which looses the quantitative accuracy when the jet is close to the breakup. Numerical results obtained using accurate numerical solutions of equation (4.10) are given below.

The numerical simulation demonstrates the influence of strong magnetic field gradients on the jet distortion. To avoid such instabilities of the mercury

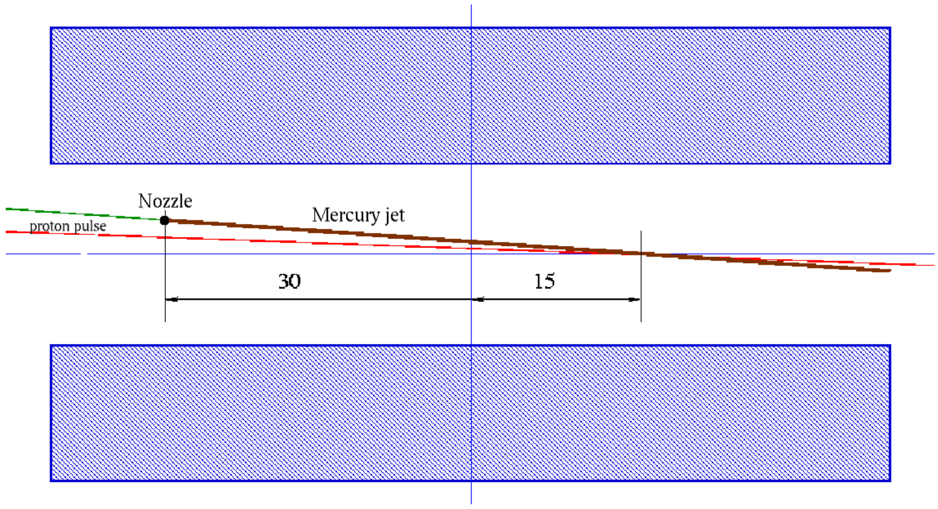

Figure 4.5: Schematic of the Muon Collider magnet.

target during its propagation in a 20 T magnetic field, the nozzle of the mercury target was placed inside the main 20 T resistive magnetic coil (see Figure 4.5). Therefore the jet will not meet strong magnetic field gradients before the interaction with the proton pulses.

We have performed numerical simulations of an off-axial mercury jet moving in 20T, 15T, and 10T solenoids using accurate numerical solution for the current density distribution (see Figures 4.7 – 4.9). Our results show that the magnetic field influence will not lead to significant jet deformations. Currently, the jet is not modeled as coming form the nozzle but is initialized as a long cylinder (see Figure 4.6). The perturbation of the tail part of the jet (Figure 4.7) is caused by the nonuniform field behind the solenoid.

Interaction of mercury jet with proton pulses

Numerical simulations presented in this section aid in understanding the behavior of the target under the influence of the proton pulse, and in estimating the evolution of the pressure waves and surface instabilities. We have neglected the influence of the external magnetic field on the hydrodynamic processes driven by the proton energy deposition.

The influence of the proton pulse was modeled by adding the proton energy density distribution to the internal energy density of mercury at a single time step. The value and spatial distribution of the proton energy was calculated using the MARS code [15]. The stiffened polytropic EOS

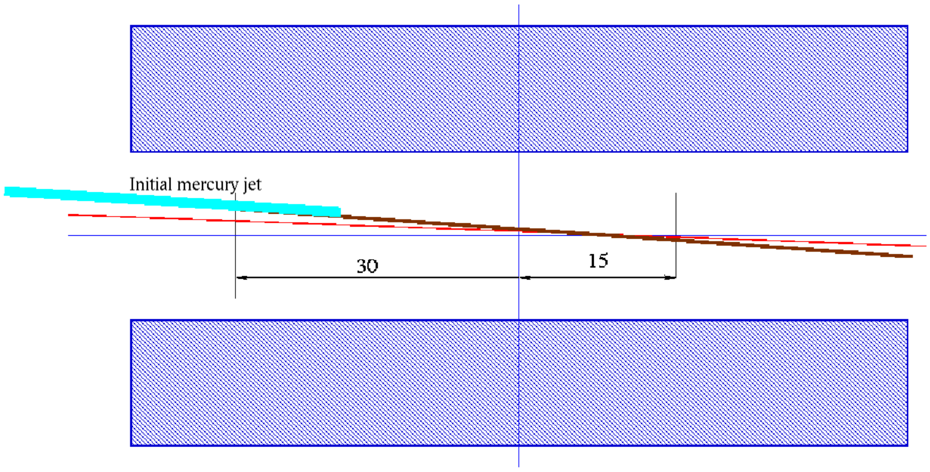

Figure 4.6: Initialization of the mercury jet.

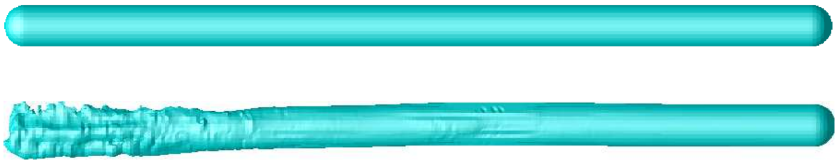

Figure 4.7: Evolution of the mercury target in 20T solenoid

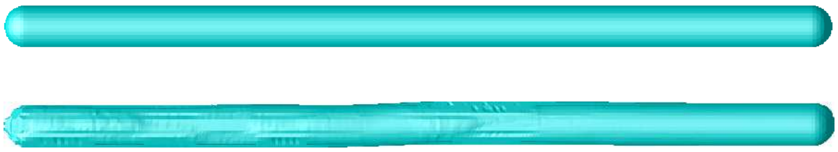

Figure 4.8: Evolution of the mercury target in 15T solenoid

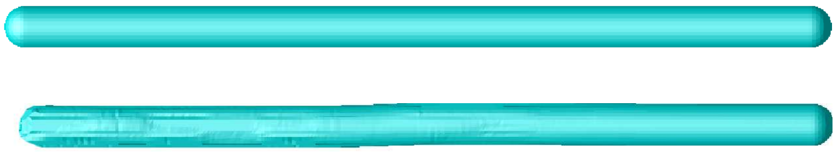

Figure 4.9: Evolution of the mercury target in 10T solenoid

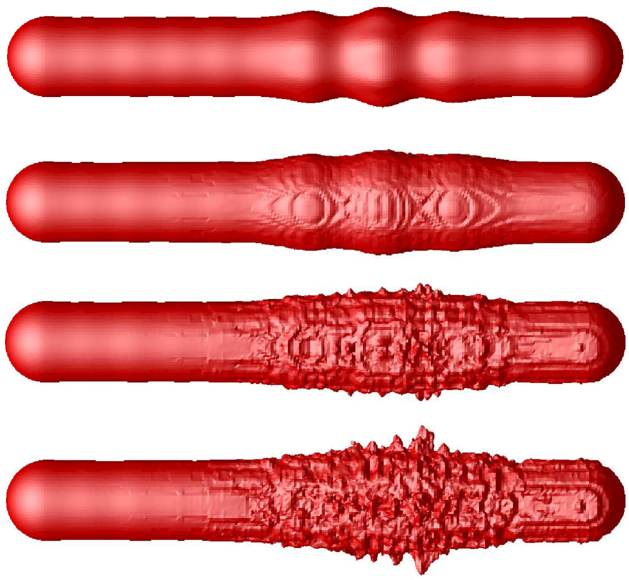

Figure 4.10: Evolution of the target driven by the proton energy deposition. Snapshots are shown at the initial time and at 27 mksec, 78 mksec, and 120 mksec.

model was used for these calculations with coefficients calculated using the tabulated EOS for mercury.

The evolution of the mercury target during 120 mks due to the interaction with a proton pulse is shown in Figure 4.10. Simulations show that velocities of surface instabilities are in the range 20 - 60 m/sec. The pressure field inside the jet developed small regions of negative pressure which indicates a possibility for the formation of cavities. Detailed studies of the cavitation phenomena in such a target will be done using the developed two-phase equation of state for mercury.

4.2 Proposed Research

In the future, we propose the following research:

- Improve the robustness of the dynamic grid generator and implement new elliptic/hyperbolic solvers.
- Develop a general analytic EOS for cavitation flows.
- Numerical simulation of nozzle effects.

- Further studies of liquid metal jets in magnetic fields.

- Numerical simulation of the mercury target interacting with a high energy proton beam in the presence of a strong magnetic field.

- Numerical simulation of turbulent jets.

Bibliography

[1] Chandrasekhar, S.: Hydrodynamics and Hydrodynamic stability. Clarendon Press, Oxford (1961)

[2] G. Chavent and J. Jaffre, Mathematical Models and Finite Elements for Reservoir Simulation. North Holland, 1986.

[3] Chern, I.R., Glimm, J., McBryan, O., Plohr, B., Yaniv, S.: Front tracking for Gas Dynamics. J. Comp. Phys. **62** (1986) 83-110

[4] Courant, R., Friedrichs, K.: Supersonic Flows and Shock Waves. Interscience, New York (1948)

[5] Glimm, J., Grove, J.W., Li, X.L., Shyue, K.M., Zhang, Q., Zeng, Y.: Three dimensional front tracking. SIAM J. Sci. Comp. **19** (1998) 703-727

[6] Glimm, J., Grove, J.W., Li, X.L., Tan, D.: Robust computational algorithms for dynamic interface tracking in three dimensions. Los Alamos National Laboratory Report LA-UR-99-1780

[7] Glimm, J., Kirk, H., Li, X.L., Pinezich, J., Samulyak, R., Simos, N.: Simulation of 3D fluid jets with application to the Muon Collider target design. Advances in Fluid Mechanics III (Editors: Rahman, M., Brebbia, C.), WIT Press, Southampton Boston (2000) 191 - 200

[8] Glowinski and M. Wheeler, Domain Decomposition and Mixed Finite Element Methods for Elliptic Problems. In R. Glowinski, G. Golub, G. Meurant, and J. Periaux, Eds., Proceedings of the First International Symposium on Domain Decomposition Methods for Partial Differential Equations, pp. 144-172. SIAM, Philadelphia, 1988.

[9] K. S. Holian, T-4 handbook of material properties data bases, Vol. 1c: Equations of state, Los Alamos Report LA-10160-MS, 1984.

[10] Kirk, H., et al.: Target studies with BNL E951 at the AGS. Particles and Accelerators 2001, June 18-22 (2001) Chicago IL

[11] Landau, L.D., Lifshitz, E.M.: Electrodynamics of Continuous Media. Addison - Wesley Publishing Co., Reading Massachusetts (1960)

[12] O. McBryan, Fluids, Discontinuities and Renormalization Group Methods. In Brittin, Gustafson, and Wyss, Eds., Mathematical Physics VII, pp. 481-494. North-Holland Publishing Company, Amsterdam, 1984.

[13] Menikoff, R., Plohr, B.: The Riemann problem for fluid flow of real materials. Rev. Mod. Phys. **61** (1989) 75-130

[14] S. Balay, W. Gropp, L. McInnes and B. Smith", PETSc Users Manual, ANL-95/11 - Revision 2.1.1, Argonne National Laboratory, 2001.

[15] Ozaki, S., Palmer, R., Zisman, M., Gallardo, J. (editors) Feasibility Study- II of a Muon-Based Neutrino Source. BNL-52623 June 2001; available at http://www.cap.bnl.gov/mumu/studyii/FS2-report.html

Chapter 5

Pulse Solenoid Concept

Chapter 6

Engineering

6.1 Mechanical Design

A three segment, layer wound solenoid is proposed for the pulsed magnet. The conductor is half inch square, cold worked OFHC copper. The coil is inertially cooled with options for liquid nitrogen or gaseous helium cooling between shots. Coolant flows through axial channels in the coil. The coil will be epoxy impregnated. Wound coils of this small radius, using cold worked conductor, retain internal elastic stresses from the winding process, and if not impregnated, require elaborate clamping mechanisms to have the coil retain it's shape.

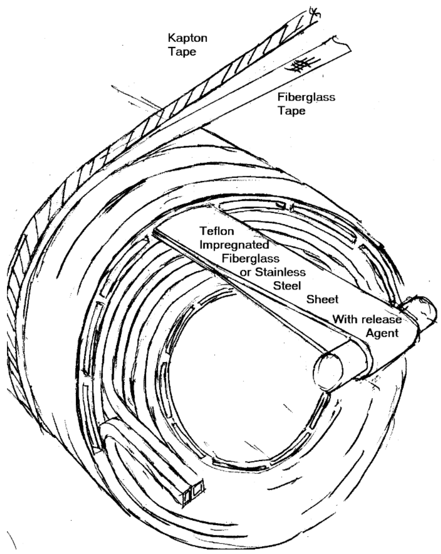

Figure 6.1: need caption here

Dual operational modes require special design of the cryostat/helium can. This is discussed in the section on cooldown behavior. Insulation design impacts the conduction cooling behavior:

- Kapton is the limiting element in the thermal conduction through the coil.
- Kapton initially was expected to be wound around the conductor. This produced the equivalent of 5 mils of Kapton between layers.

Table 6.1: Proposed Operational Scenarios

Case No.	Peak Field (T)	Coolant	T after pulse (K)	T coolant (K)	Start Bulk Temp (K)
1	5	Helium Gas	90	66	84
1a	5	LN2	90	66	84
2	10	Helium Gas	96	66	74
2a	10	LN2	96	66	74
3	15	Helium Gas	78	22	30

- To improve conduction, Kapton is used only between the layers. Turn to turn voltage is lower than layer to layer. The turn to turn voltage is less than the rule of thumb for He breakdown voltage (1 volt/mil at 1 atmosphere) for the insulation thickness proposed. Note that the He operating pressure is expected to be 15 atmospheres, the pressures inside the epoxy winding pack may be substantially lower, depending on Helium diffusion, making the 1 atm breakdown voltage for the conductor, reasonable.

- The layer to layer voltage exceeds this rule of thumb, however, and would need the Kapton if there was an imperfection in the epoxy/glass insulation. Half laps of kapton and fiberglass, similar to the CS model coil will retain some structural integrity.

- Once a layer of conductor is wound, a layer of Kapton/glass would be wound on the completed layer of conductor. This produces the equivalent of 3 mils of Kapton rather than 5 if the conductor were wrapped individually. Every 6 to 8th layer some sort of preformed channel array would be layed on, then wrapped with glass/Kapton to hold it in place, and as the layer insulation for the next layer of conductors.

Experience with Alcator C-Mod indicates that for final magnet temperatures at or below 100K, the channels will not need ”turbulators” or surface trips to break-up the film boiling layer. This will have to be reviewed during the design phase. If some form of surface roughness will be required in the 2mm channels, then the method of forming the channels with removable strips will have to be re-visited.

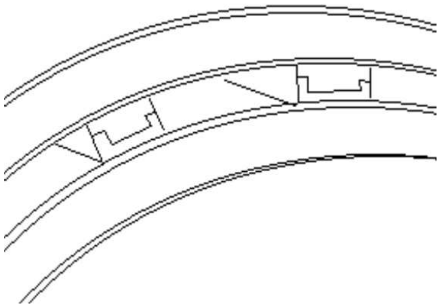

Figure 6.2: Ribs that form the channels may need to have sliding parting planes to allow axial and radial motion between coil segments.

6.2 Engineering Tasks

While the magnet has been conceptualized, with some analytic basis, detailed engineering will require additional work after the construction of the magnet is approved. These tasks are outlined below.

- Identify Voltages for All Operating Scenarios - Choose insulation systems. Determine where Kapton is used.
- Stress Analysis, Assess radial load on channel ligaments, consider operation with inner modules energized, and no current in outer module
- Confirm cooldown and pressure drop calculations
- Analyze thermal contraction/shock of channel - Avoid separation and loss of conduction
- Design He can for 15 atm. and vacuum operation.
- Design mandrel and flow plenums
- Cryostat Design. Is this a Vacuum Cryostat with LN2 Shield, or a Gaseous N2?

- Break-outs and Leads Penetration design - Design the required support to resist loads and torques that result from principally the end radial Field.
- Determine if Eddy Currents in He Can represent a significant load.
- Design Cryogenic Electrical Breaks
- Design Supports, Break-outs, He can and Cryostat to Allow Phased Construction

Some of the analytic work in support of the present design is now described:

6.3 Stress Analysis

The coil is stress analyzed using ANSYS. Fields and forces are computed using elliptic integrals in a code external to ANSYS. The model is axisymmetric. Figures 6.3 - 6.7 show a 3D representation from a symmetry expansion.

Table 6.2: Coil Build used in the Stress Analysis

Seg No.	r	z	dr	dz	nx	ny
1	0.15	0	0.098	1.0	16	16
channel	0.2	0	0.002	1.0	1	16
2	0.25	0	0.098	1.0	16	16
channel	0.3	0	0.002	1.0	1	16
3	0.35	0	0.098	1.0	16	16

For Fusion magnets the inner skin of the solenoid is allowed to reach the yield - Treating this stress as a bending stress with a 1.5*Sm allowable with Sm based on 2/3 Yield.

Table 6.3: Interpolated values:, Work hardened copper-, OFHC c10100 60% red

temp deg K	77	90	100	125	150	200	250	275	292
yield	374	369.	365.	356.	347.	328.	317.	312.	308.
ultimate	476.	466.	458.	439.	420.	383.	365.	356.	350.

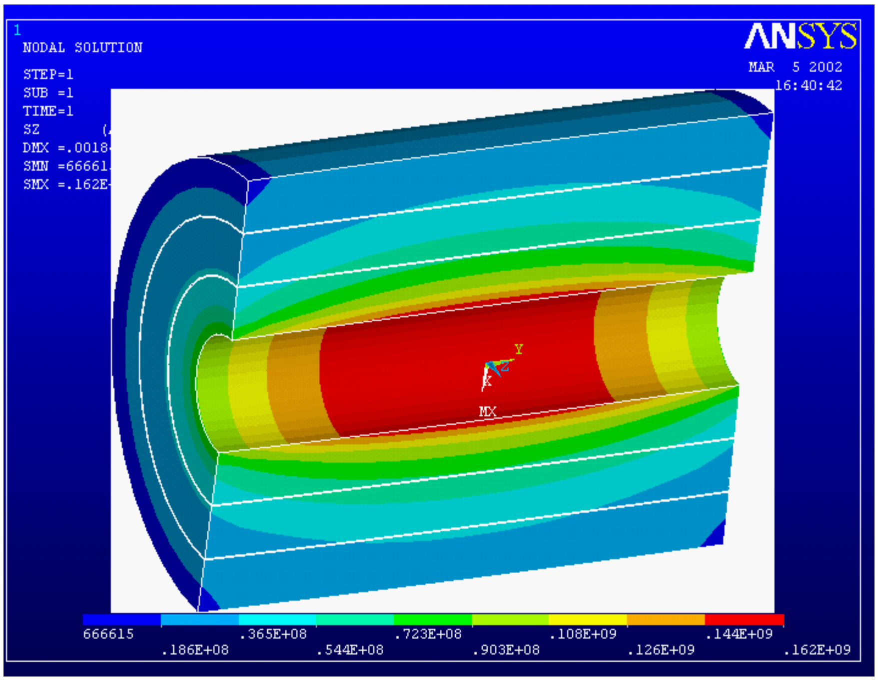

Figure 6.3: Hoop stress, all coil segments fully energized. The Von Mises stress plot is similar with a peak of 165 MPa, Tresca is 166 MPa.

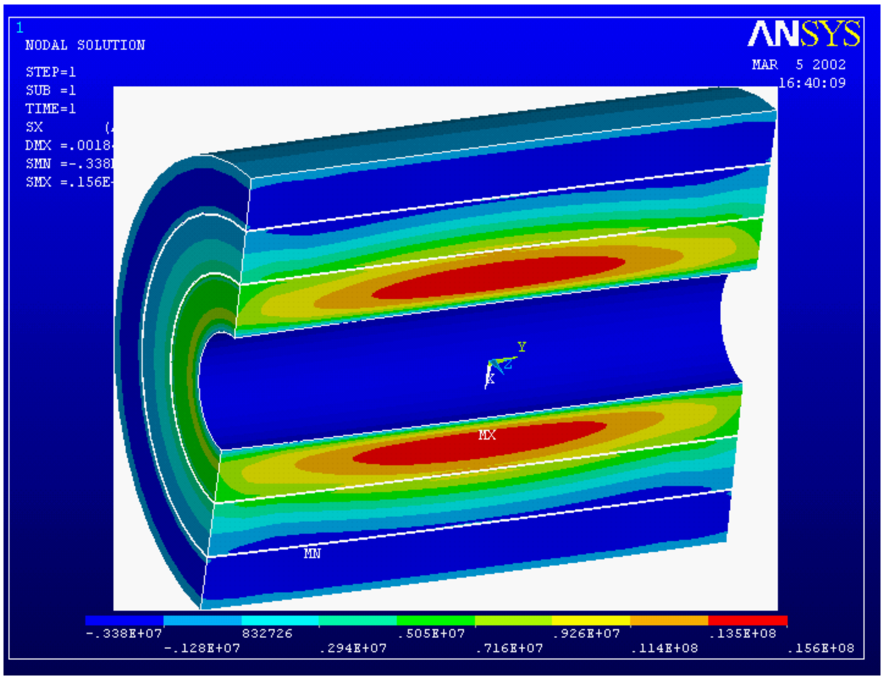

Figure 6.4: Radial tension stress, all coils fully energized. There is about an MPa of tension at the boundary between the first and second module. To avoid damage to the channel ligaments, a parting plane will be incorporated in the channel detail. This needs to occur in the ligament to retain thermal connection with the coolant in the channel.

If the highly cold-worked copper is chosen for the winding, the conductor allowable near the inside radius of the coil would be 365 MPa. The max stress in the three segment coil is 166 MPa. With this stress level, it is expected that half hard copper could be used, simplifying the winding process.

The three segment coil has three operational modes, two of which are structurally significant. The full performance configuration is limiting in terms of hoop stress and equivalent stress. It also has some radial stresses that will have to be mitigated with parting planes at the segment boundaries, or within the winding.

In the initial operating mode the outer coil segment is not energized. This induces some differential Lorentz forces and differential temperatures, that cause shear stresses between segments.

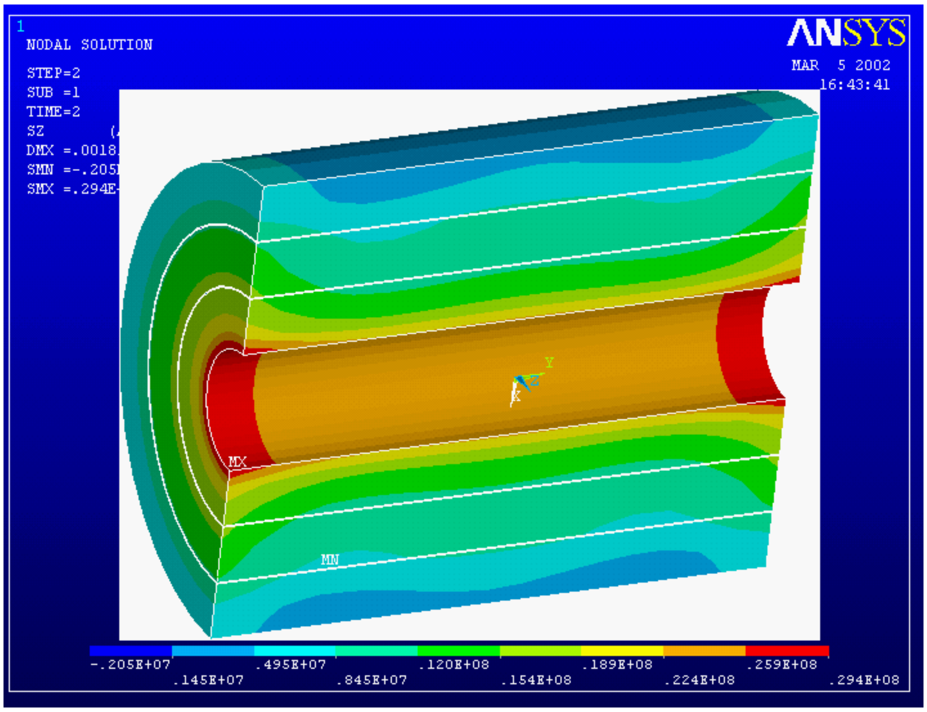

Figure 6.5: Hoop stress with only the inner two segments energized.

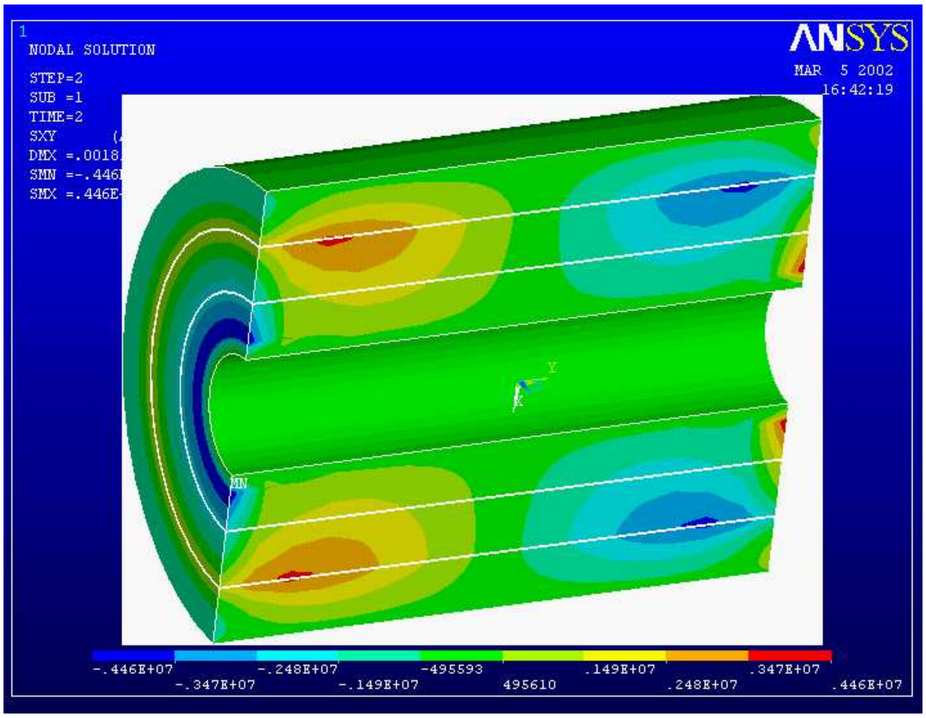

Figure 6.6: Smeared radial-axial stress with the inner two segments energized. This is a peak at the interface between the second and third modules. It must be carried across the thin ligaments between the channels, or relieved via a slip plane.

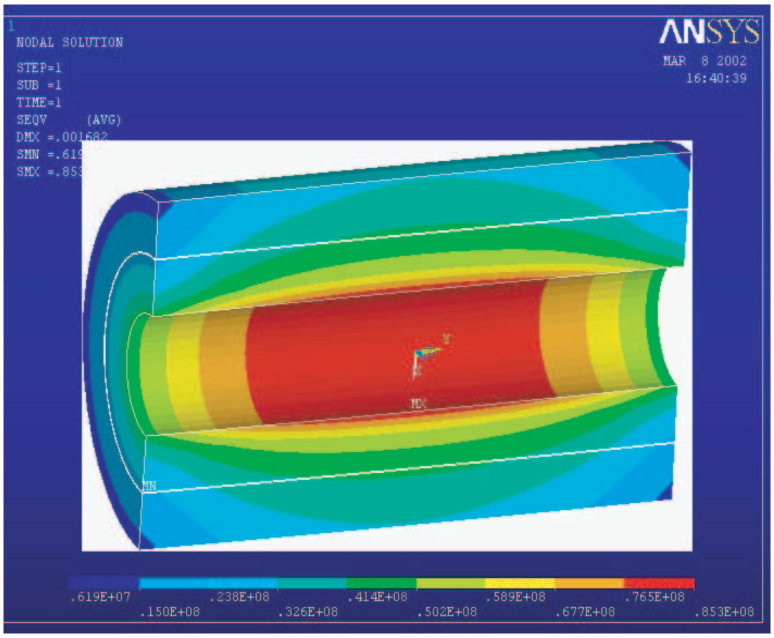

Figure 6.7: write caption

It may be desirable to build only the initial two inner segments and add the outer segment at a later time. The coil was analyzed with the outer segment removed, and the same current density in the other two segments. The max stress for this case is 85.3 MPa, which is a bit more than with the outer segment in place, but less than for the fully energized three segment coil. In all cases the stresses are lower than the expected allowable for the conductor. It is expected that the degree of cold work can be relaxed from the full hard condition. The final choice of the degree of cold work for the conductor will be determined during detailed design.

6.4 Cooldown Between Shots

Phased implementation of cooling systems is expected for the project. Within the coil, two cooldown methods are being investigated: and option using liquid nitrogen and an option which uses helium gas. It is expected that design of the magnet and cooling channels will allow either working fluid. Use of liquid nitrogen as the only coolant is contemplated for the initial operation of the magnet. It is possible to use the container around the magnet as a vacuum vessel, and sub-cool liquid nitrogen to 66 K. Helium gas operation uses liquid nitrogen to cool the helium gas in a heat exchanger, and later allows use of liquid hydrogen to cool the helium and obtain improved fields and/or pulse lengths. The heat transfer characteristics of liquid nitrogen operation have only been conceptualized. Heat transfer calculations using gaseous helium will be presented here.

In the LN2 sub-cooling mode, about 50 cubic meter of nitrogen gas at standard temperature and pressure must be drawn off by the vacuum pump to lower both the magnet and the liquid nitrogen to the desired 66 K temperature.

6.5 Cooling Time with Helium Gas as a Working Fluid

The solenoid has groups of 6 to 8 layers of 1/2 inch square conductors separated by set of annular cooling channels. This could model any linear stack of .5 inch square conductors cooled from the ends of the stack whether layer wound - then there would be a layer of channels every sixth layer of conductor, - or pancake wound, where there would be radial channels every sixth pancake. The solution is a simple finite difference transient analysis. The ground wrap or cracked conductor/Kapton tape interfaces have not been modeled.

The insulation layer is modeled with five, and as a second option, three, 0.001" thicknesses of Kapton tape. The thermal conductivity of the tape is about 0.14 W/(m-K) at 100 K [1].

The surface heat transfer coefficient at the channels was taken as 170 W/m^2 for nitrogen gas at 100 K flowing at 40 m/s in a channel with a 2 cm hydraulic diameter [2]. The helium gas coefficient has been calculated from the Nusselt, Reynolds, and Prandle Numbers using the relation quoted in the Oak Ridge document [3], and will be verified during detailed design.

Typical results for 66 K He cooling, 0.1 kg/sec, 100 K end of pulse temperature 85 K target magnet start temperature. The cooldown time is 600 s. to reach 85 K bulk temp, but not thermal equilibrium.

From $\dot{m} \times C_p \times \Delta T$ for a 20 deg inlet-outlet difference the cooldown time is about 950 s. The simulation with a finer time step ($\delta time = 0.0001$ rather

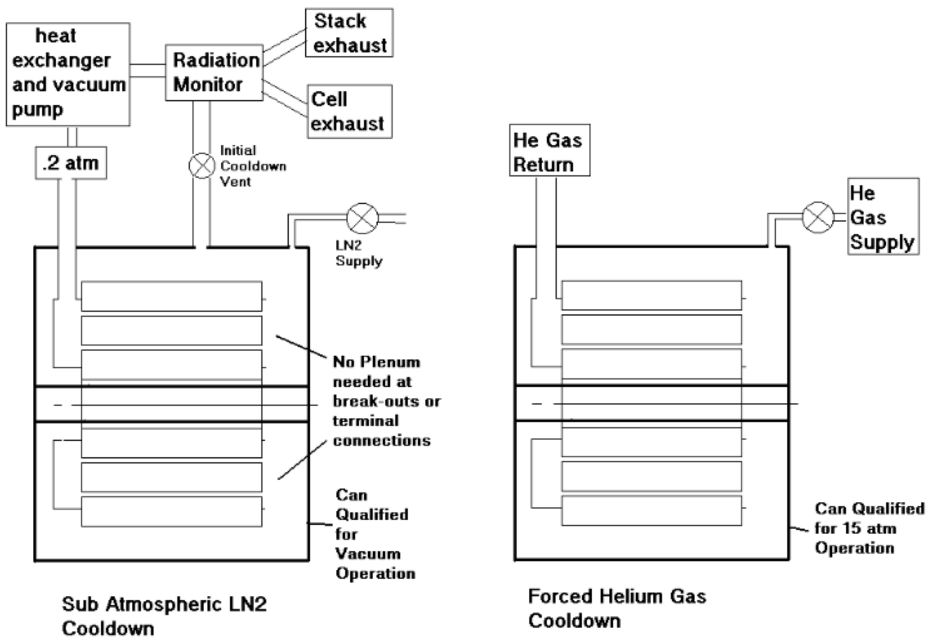

Figure 6.8: Proposed operational modes. The coil and can are designed for either cooling mode.

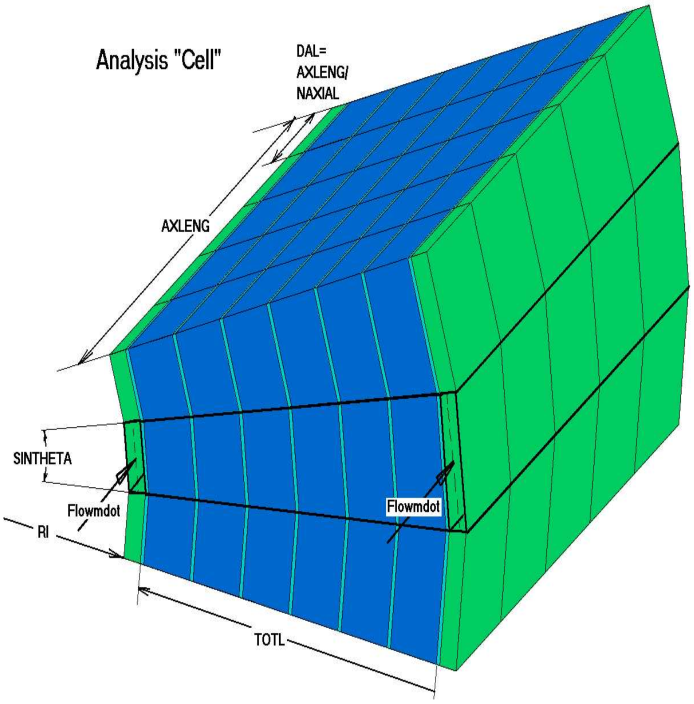

Figure 6.9: write caption

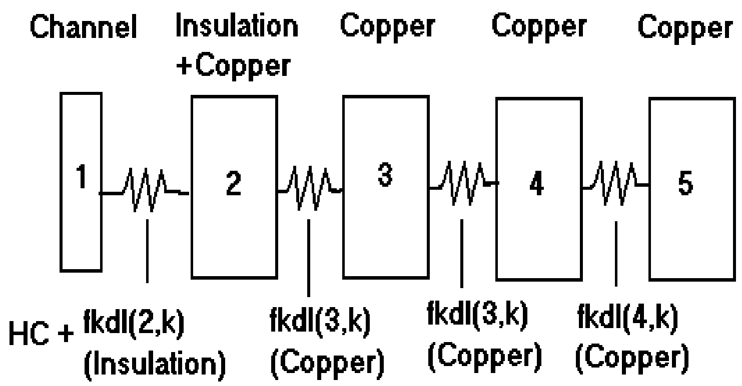

Figure 6.10: write caption

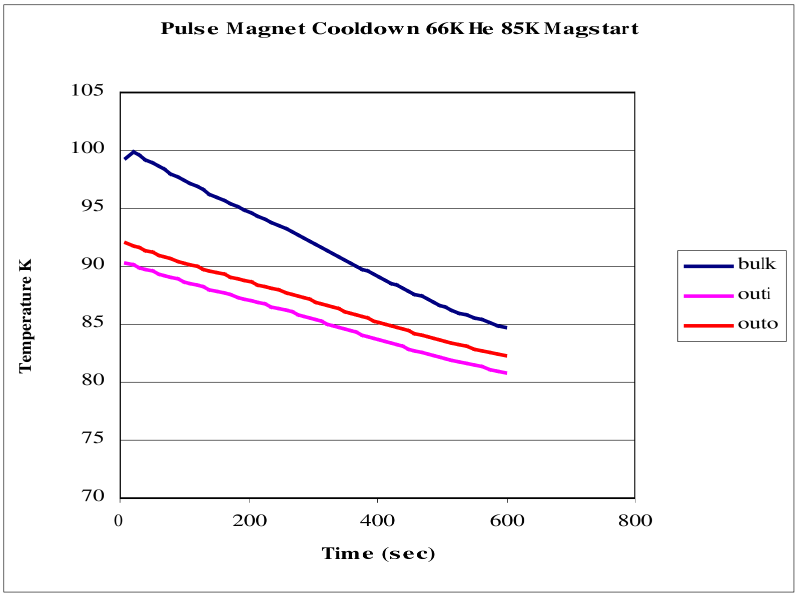

Figure 6.11: Temperature *vs.* time in seconds.

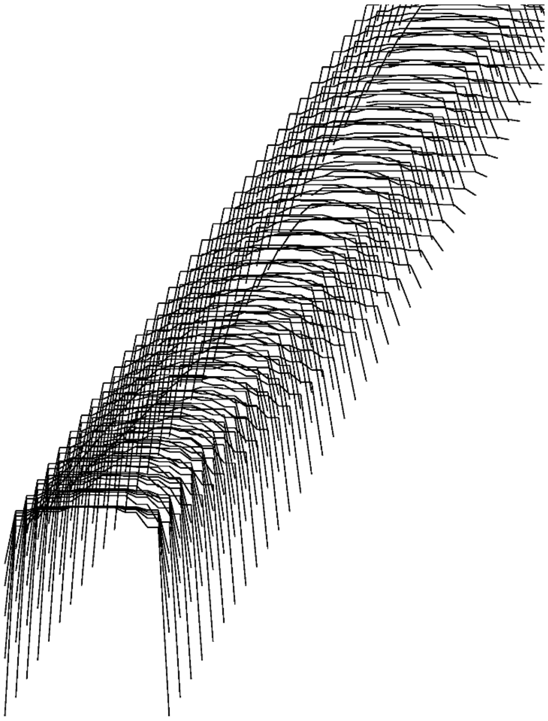

Figure 6.12: *Cell* temperature profiles. Time progresses towards the upper right. The groups of plots are temperature profiles for the five axial stations for which the temperature are calculated.

Table 6.4: Present Operational Scenarios

Case No.	Peak Field	T after pulse	T coolant	Start Bulk Temp	Guesstimated Time
1	5T	90K	66K	84K	200 s
2	10T	96K	66K	74K	800 s
3	15T	78K	22K	30K	1500 s

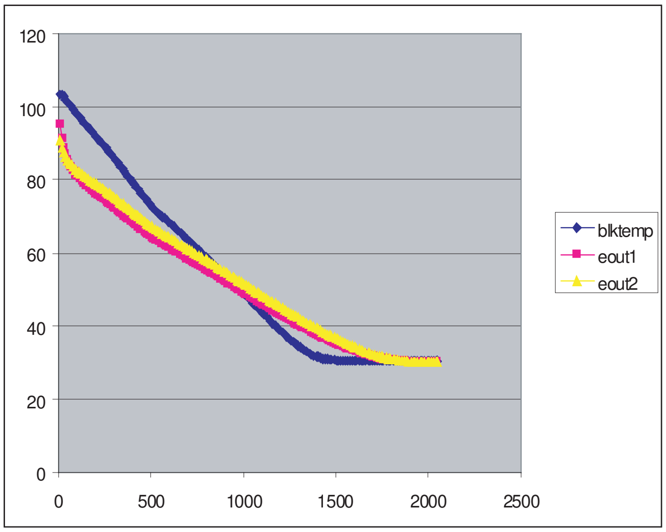

Figure 6.13: Temperature *vs.* time in seconds. Tout1 and Tout2 are outlet temperatures.

than 0.001) yields a 600 s cooldown . The inlet outlet ΔT ranges from 26 K to 16 K. The energy balance or difference between the conduction heat flux and the channel heat flux is good at the finer time step.

6.6 30 K Coolant, Cooldown from 100 K

Bulk temp is computed as the average temperature at mid axial build. It bottoms out before the down stream end. In the plot above, the channel outlet temperatures are better indicators of when the magnet reaches 30 K

Table 6.5: Parameters

Number of Atmospheres Operating Pressure	10
Enter Channel Height (mm)	2
$R_{\mathrm{i}nner}$	0.1000000
radial build	7.6200157×10^{-2}
inner coil start temp	100.0000
outer coil start temp	100.0000
inner coil radius	0.1000000
model cell energy (J)	1644.685 (100 to 85 K bulk)
model cell volume	5.5099601×10^{-5}
volume cpp	1989954.0
nlength	120
naxial	5
Mass flow rate	4.1666666×10^{-5} kg/s
Volume flow rate	5.5507730×10^{-6}
flow velocity	2.120239
Hydraulic Diameter	2.8944151×10^{-3} m
Velocity Head	1.721665 Pascal
Pressure Drop	31.46283 Pascal
Pressure Drop	3.1041747×10^{-4} Atmospheres
Helium density	7.506462 kg/m^3
Helium viscosity	2.6448268×10^{-7}
Prandl #	4.0756337×10^{-2}
Reynolds #	174174.1
Heat transfer coefficient	115984. 9

Table 6.6: Analysis to date: Time to target bulk temp from 100 K. $\frac{1}{2}$ inch Copper Conductor.

	T after pulse K	T coolant K	Cond. Layers	Time to 85 K s	Time to 30 K s
Equiv 5 Kapton 0.001 in wrap	100	66	6 layers	600	xxx
Equiv 5 Kapton 0.001 in wrap	100	66	8 layers	850	xxx
Equiv 3 Kapton 0.001 in wrap	100	66	8 layers	450	xxx
Equiv 5 kapton 0.0001 in wrap	100	30	6 Layers	2000	xxx

Bibliography

[1] Rule, Smith, and Sparks, *Thermal Conductivity of Polymide Film between 4.2 and 300K with and without Alumina Particles as Filler*, NISTIR #3948. August 1990.

[2] Oak Ridge CIT report # ORNL/FEDC-85-10 Dist. Category UC20 c,d October 1986.

[3] Excerpts from reference [2]

2.1.3 Convective Heat Transfer

It is important to estimate how much heat the superheated nitrogen gas ($T > 77\ K$) could absorb before exiting the cooling channel. The convective heat transfer coefficient, h, could be obtained from

$$h = \frac{KNu}{D_e} = \frac{0.023 R_e^{0.8} P_r^{0.4} K}{D_e}.$$

This coefficient is about 21×10^{-3} W/cm^{2}K at a vapor temperature of 200 K, vapor velocity of 40 m/s, and hydraulic diameter of 2 cm. It drops to 17×10^{-3} W/cm^{2}K at a vapor temperature of 100 K, keeping the mass flow rate constant. It is interesting to note that the heat transfer coefficient for film boiling at 200 K from Fig. 4 is about 12×10^{-3} W/cm^{2}K, which partially justifies the third assumption in Sec. 2.1.

6.7 Coil Package

6.8 Cryogenic System

6.9 Power Supply System

6.9.1 Experiment E951 Power Supply to Pulse a 14.5 T Solenoid Magnet

Introduction

The project goal is to pulse a magnet with 20 cm diameter bore, capable of a peak field near 15 T and a repetition rate of about 30 minutes.

Funding realities make it prudent to consider a stageable design with the following 3 cases

- The magnet achieves peak field of 5 T 84 K
- The magnet achieves peak field of 10 T 74 K
- The magnet achieves peak field of 14.5 T 30 K

Table 6.7: Parameters of Pulse Magnet System with 1 sec flat top

	Case 1	Case 2	Case 3
Outer radius (cm)	30.0	30.0	40.0
Copper mass (kg)	1943	1943	3644
Voltage (V)	150	300	300
Peak current (A)	3600	7200	7200
Field (T)	5.0	10.0	14.5
Inductance (mH)	138	138	436
Initial temperature (K)	84	74	30
Time t1, to end of flat tap (s)	8.2	7.3	16.3
Pulse length at tp (s)	11.1	10.1	24.1
Initial Resistance (mOhms)	30.2	23.5	11.0
Resistance at t1 (mOhms)	34.1	35.3	33.0
Resistance at tp (mOhms)	34.1	37.2	38.2
Dissipation at tp (mJ)	2.70	9.1	15.2

Cases 2 and 3 require the same power supply, but differ in the magnet cooling scheme.

From the power supply point of view, we will start with a 540 KVA power supply rated at 3600 A, ±150 V (Case 1)

To support case 1, and for cases 2 and 3 we will have four 540 KVA in series/parallel to generate 7200 A, ±300 V (Cases 2-3).

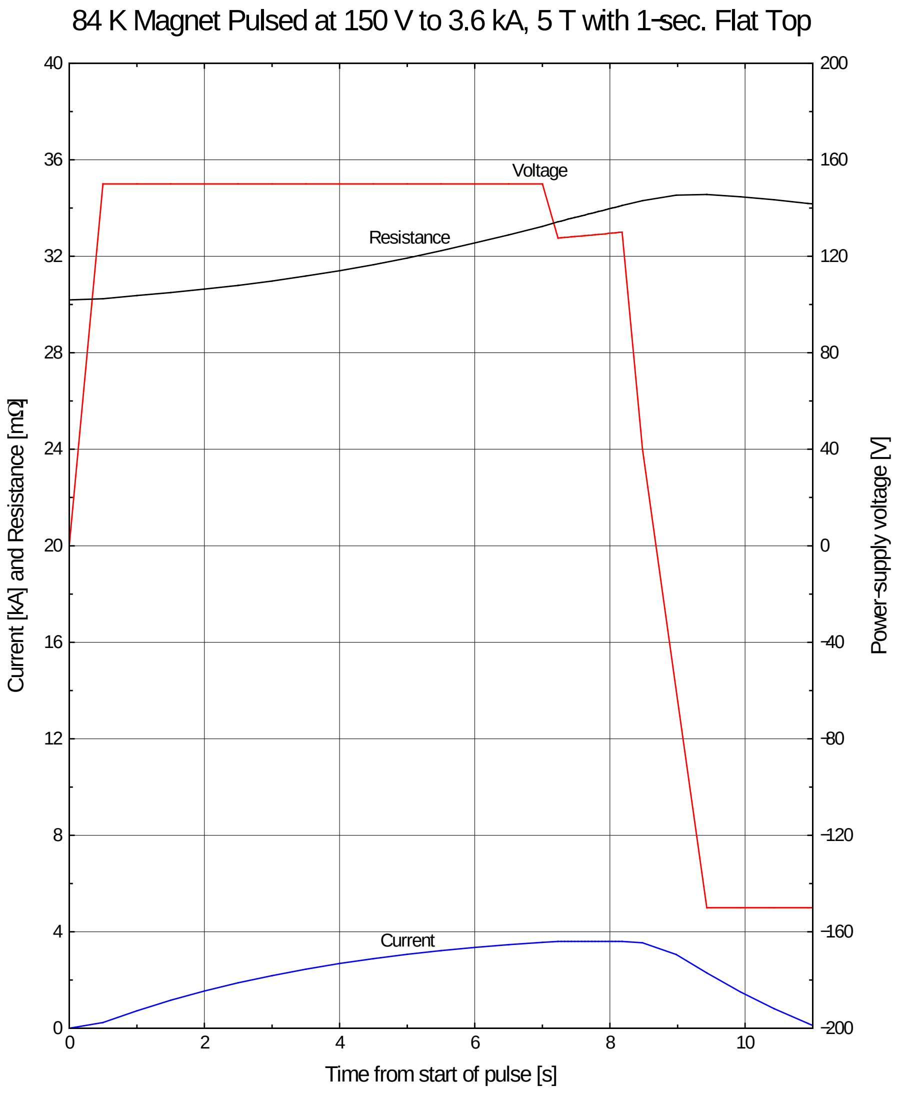

Figure 6.14: Performance of the 5 T magnet with the Case 1 power supply

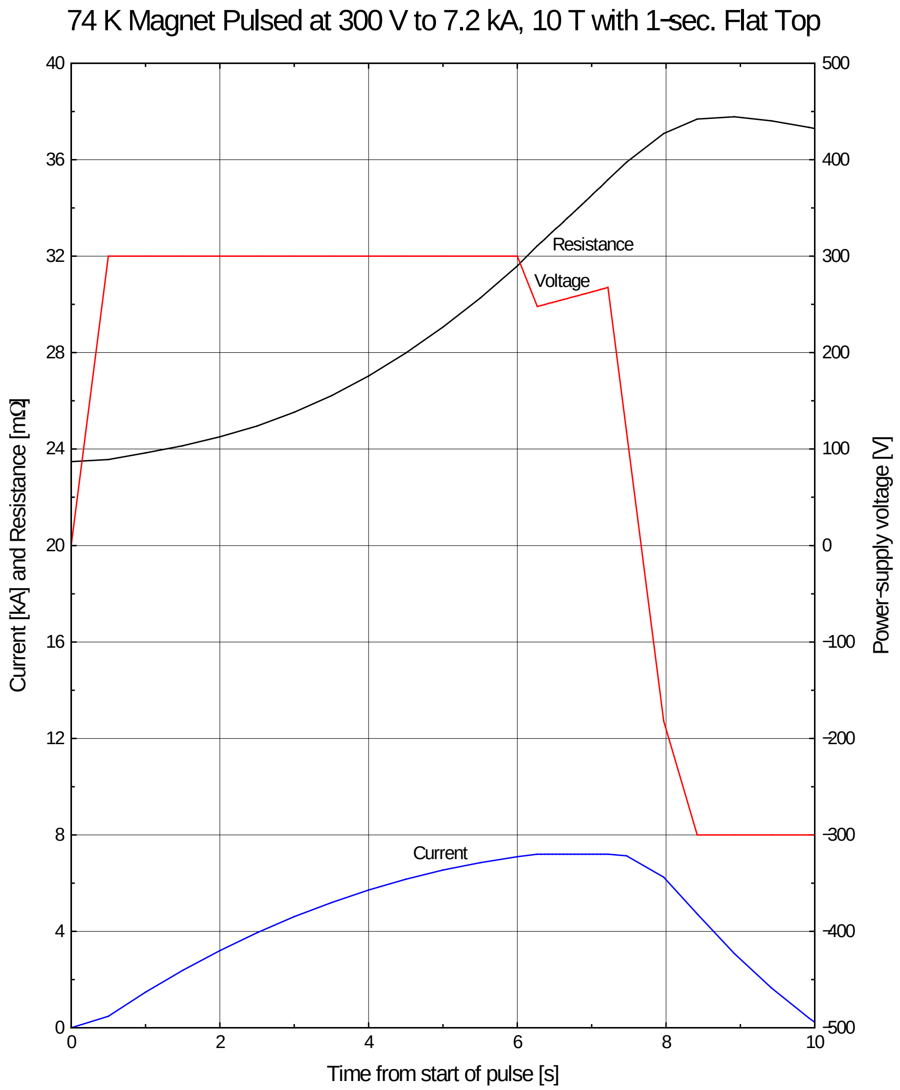

Figure 6.15: Performance of the 10 T magnet with the Case 2 power supply

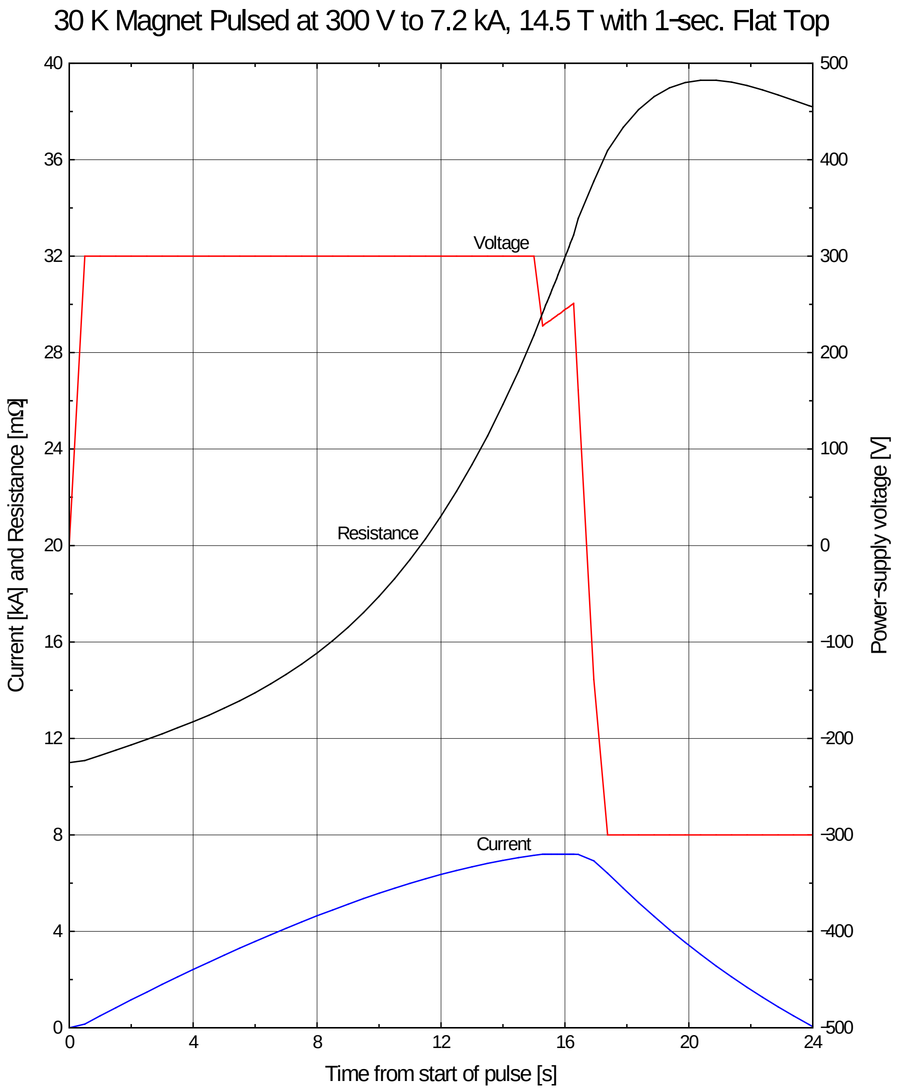

Figure 6.16: Performance of the 14.5 T magnet with the Case 3 power supply

The 540 KVA power supplies are thyristor-control six-pulse rectifiers, available at BNL from previous experiments.

These power supplies are presently configured as DC power supplies.

We need to modify their regulators to be able to pulse them.

The controls and interlocks of these power supplies must be updated.

Similar upgrades have been made during the Booster project with great success.

Case 1 power supply (5 T magnet)

This power supply will be a thyristor phase control power supply rated at 3600 A, $\pm$150 V.

This power supply exists at Brookhaven from previous experiments.

The 3-phase, 480 V input power will be fed from an existing disconnect switch.

The power supply will have an AC circuit breaker.

A new regulator will be implemented based on the existing design for the AGS Main magnet power supply.

The power supply will be fully programmable from 0 to 3600 A.

It will have a voltage regulator as the inner loop and a current regulator as the outer loop.

Both voltage reference and the current reference will be generated from a high-level computer algorithm for a given magnetic field pulse and a given function of the load resistance as a function of current and time.

We need to replace the voltage feedback sensor with a LEM DCPT (DC potential transformer).

We need to replace the existing current sensor (shunt) with a LEM DCCT (DC current transformer).

These sensors have been successfully used in the past in various power supply systems.

All the old interlocks will be updated using an Allen Bradley Programmable Logic Controller (PLC).

This PLC will be programmed to make decisions on the interlocks and safely turn of the power supply if an interlock occurs.

The power supply will have the following interlocks:

- DC Over-current
- RMS magnet current interlock

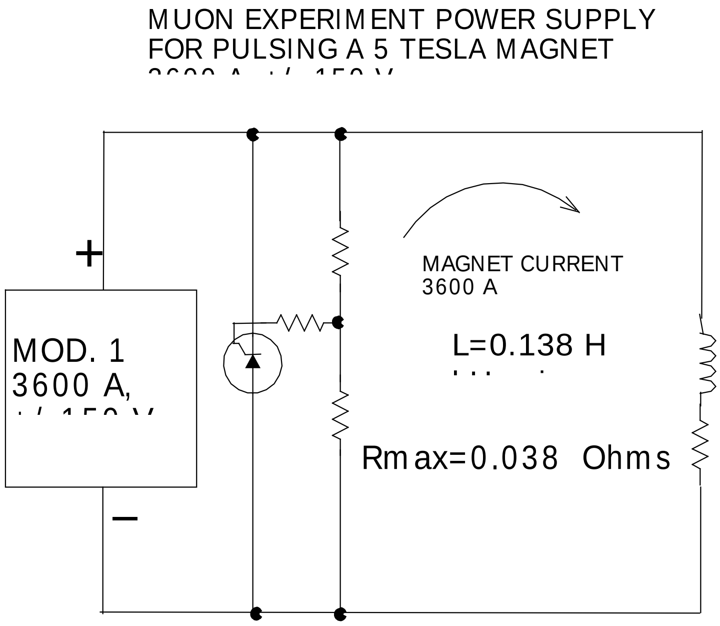

Figure 6.17: Need caption

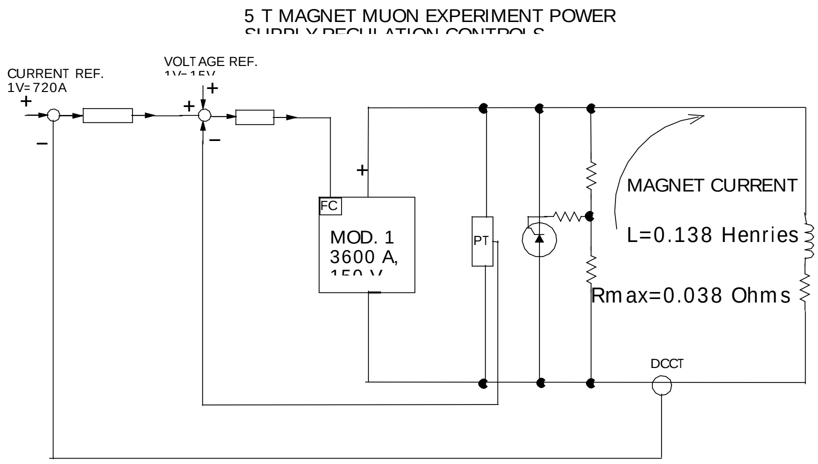

Figure 6.18: Need caption

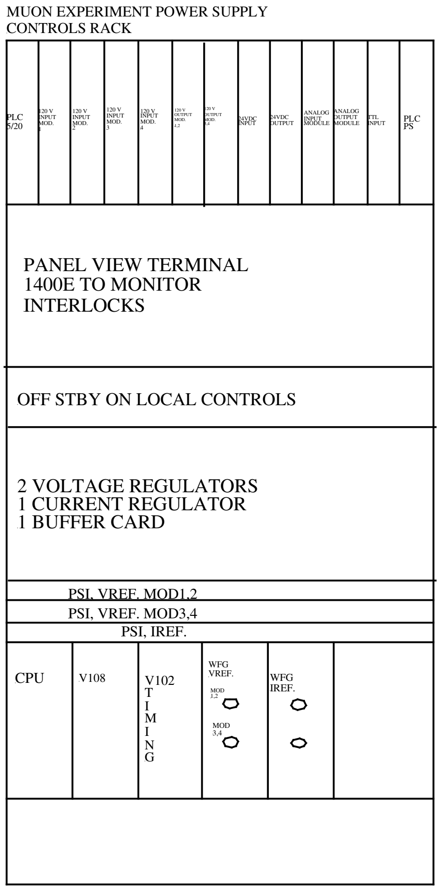

Figure 6.19: Need caption

- AC Over current
- Blower failure
- Ground Fault
- Magnet faults
- Magnet resistance interlock
- Cryo-interlocks

In case of any interlock failure, the power supply will be phased to 150 degrees in 100 ms.

This means the power supply voltage will be -150 V, the current then will go to zero in 3 s maximum time, depending where the interlock occurs in the cycle.

Then the AC circuit breaker will be commanded to open by the PLC regardless whether the magnet current is at zero or not.

A crowbar circuit based on self-triggering silicon control rectifiers (SCR's) will be implemented to short the magnet if the magnet voltage becomes greater than 350 V.

In this case, the magnet current will decay to zero with the L/R magnet time constant which is typically 3.6 s.

Note: L = 138 mH, $R_{\mathrm{max}} = 38\ m\Omega$. Minimum repetition rate is 5 minutes

Case 2-3 power supply (10, 14.5 T magnet)

This power supply will be a thyristor phase control power supply composed of 4 series/parallel Case-1 power supplies. It will be rated at 7200 A, ±300 V.

These power supplies exists at Brookhaven from previous experiments and will be modified as described in Case 1.

The 3-phase, 480 V input power will be fed from existing disconnect switches.

The power supply will have four AC circuit breakers, one per power supply.

Two parallel power supplies (MOD 1 and MOD 2) will be fed from the same existing substation and the other two (MOD 3 and MOD 4) from a different existing substation. This will not require any modifications to our existing substations regarding power supply input power requirements.

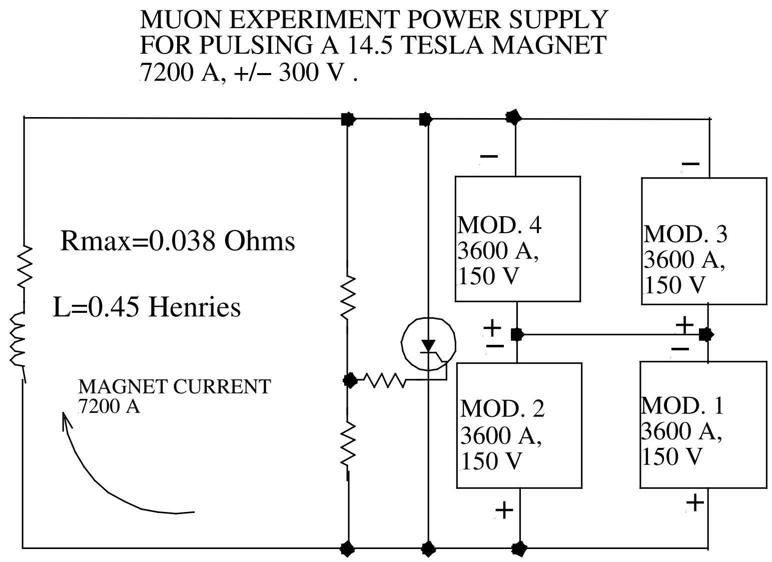

Figure 6.20: Case 2-3 power supply (10, 14.5 T magnet)

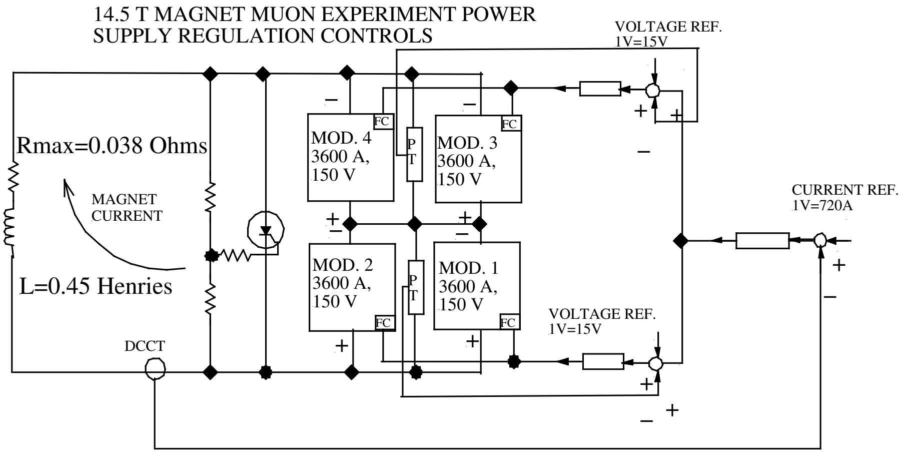

Figure 6.21: Case 2-3 power supply (10, 14.5 T magnet)

The power supply will be fully programmable from 0 to 7200 A.

It will have two voltage regulators as the inner loops and a current regulator as the outer loop.

Note: For Case 2, L = 0.138 H, $R_{\rm max} = 38\ m\Omega$, for Case 3, $L = 0.436\ H$, $R_{\rm max} = 37\ m\Omega$.

In order to share current properly between parallel power supplies, we intend to run 2-in water-cooled busses from the + terminal of MOD 2 to the magnet and from the + terminal of MOD 1 to the magnet. The same is true for the - terminal of MOD 4 and MOD 3.

The anticipated overall bus resistance should not exceed 2 $m\Omega$.

A crowbar circuit based on self-triggering silicon control rectifiers (SCR's) will be implemented to short the magnet if the magnet voltage becomes greater than 350 V.

In this case, the magnet current will decay to 0 A with the L/R magnet time constant which is typically 3.6 s for Case 2 magnet, 12 s for Case 3 magnet.

All the old interlocks will be the same as Case 1 power supply and will be updated using an Allen Bradley Programmable Logic Controller (PLC).

Minimum repetition rate for case 2 magnet is 20 minutes, for case 3 magnet 30 minutes.

Table 6.8: Schedule

Muon Power Supply Schedule (1-29-02)			
Quarters	Design & Development	Fabrication	Installation/Commissioning
1	Design for Case 1	Procurement	
2		Fabrication of Case 1	
3			Installation of Case 1
4			Commissioning of Case 1
5	Design for Case 2,3		
6		Fabrication of Case 2,3	
7			Installation of Case 2,3
8			Commissioning of Case 2,3

The Case 1 power supply should be compete by the end of the 4rd quarter, middle of FY03.

The Case 2-3 power supply should be complete by the end of the 8th quarter, middle of FY04.

This schedule is spread apart over 2 years, taking into account other projects of the C-AD Power Supply Group.

All the parts purchased should be bought at the same time for the following reasons:

- We need almost all the parts for the controls rack for Case-1 power supply.
- The DC bus should be bought at the same time to save money.

Cost estimate

Table 6.9 includes burden of 87% on labor and burden of 47% on materials.

Table 6.9: Cost Estimate

Muon Power Supplies				Duration (man days)			
Description	$ Labor	$ DTS	$ Purch	Engr	Dsgn	Tech	$ DTS
MUON PS - 1 Design & Development	33469						
Case 1 PS 3600 A, ±150 V	19461	0	0	13	8	4	0
Case 2,3 PS 7200 A, ±300 V	14008	0	0	8	8	3	0
Muon PS - 2 Fabrication	82353	145383					
Case 1 PS 3600 A, ±150 V	45369		145383	31	0	25	0
Case 2,3 PS 7200 A, ±300 V	36983		0	15	0	33	0
Muon PS - 3 Installation	84116	4034					
Case 1 PS 3600 A, ±150 V	29557	1008	0	10	0	29	1.5
Case 2,3 PS 7200 A, ±300 V	54558	3026	0	15	0	57	5
AMOUNT FOR CASE 1	94388	1008	145383				
TOTAL CASE 1	240780						
TOTAL WITH 20% CONTINGENCY	288936						
AMOUNT FOR CASES 2,3	105550	3026	0				
TOTAL CASES 2,3	108575						
TOTAL WITH 20% CONTINGENCY	130290						
TOTAL AMOUNT	199938	4034	145383				
TOTAL NO CONTINGENCY	349355						
TOTAL WITH 20% CONTINGENCY	419226						

6.10 Environment, Safety and Health Considerations

Chapter 7

Cost and Schedule

Chapter 8

R & D Plans

Bibliography

[1]